

Proximity-Coupling-Induced Significant Enhancement of Coercive Field and Curie Temperature in 2D van der Waals Heterostructures

Luman Zhang, Xinyu Huang, Hongwei Dai, Mingshan Wang, Hui Cheng, Lei Tong, Zheng Li, Xiaotao Han, Xia Wang, Lei Ye,* and Junbo Han*

Magnetism in 2D has long been the focus of condensed matter physics due to its important applications in spintronic devices. A particularly promising aspect of 2D magnetism is the ability to fabricate 2D heterostructures with engineered optical, electrical, and quantum properties. Recently, the discovery of intrinsic ferromagnetisms in atomic thick materials has provided a new platform for investigations of fundamental magnetic physics. In contrast to 2D CrI_3 and $\text{Cr}_2\text{Ge}_2\text{Te}_6$ insulators, itinerant ferromagnetic Fe_3GeTe_2 (FGT), which has a larger intrinsic perpendicular anisotropy, higher Curie temperature (T_C), and relatively better stability, is a promising candidate for achieving permanent room-temperature ferromagnetism through interface or component engineering. Here, it is shown that the ferromagnetic properties of FGT thin flakes can be modulated through coupling with a FePS_3 . The magneto-optical Kerr effect results show that the T_C of FGT is improved by more than 30 K and that the coercive field is increased by $\approx 100\%$ due to the proximity coupling effect, which changes the spin textures of FGT at the interface. This work reveals that antiferromagnet/ferromagnet coupling is a promising way to engineer the magnetic properties of itinerant 2D ferromagnets, which paves the way for applications in advanced magnetic spintronic and memory devices.

Since the discovery of intrinsic 2D ferromagnetism in atomic thick CrI_3 and $\text{Cr}_2\text{Ge}_2\text{Te}_6$ crystals, various types of van der Waals (vdW) 2D ferromagnets (FMs) have been grown and explored.^[1–6] By fabricating crystals containing different layers

and constructing heterostructures with multiple functional vdW blocks, many fundamental physics characteristics and new device functions have been investigated.^[7–11] However, most of the observed 2D FMs only have long-range order at low temperatures, it is therefore crucial to increase the Curie temperature (T_C) of the FMs to meet the requirements of industrial applications, before new room-temperature 2D FMs would be found. Many techniques, including straining, electric fields,^[12–15] gating,^[16] pressure,^[17,18] and proximity coupling,^[19–28] are usually used to modulate the performances of the devices. Among these methods, the proximity coupling effect is an effective way to promote the magnetic properties of FMs without requiring any external energy consumption. For example, the FM EuS magnetic property persisted to room temperature when the heterostructure $\text{Bi}_2\text{Se}_3\text{-EuS}$ was fabricated.^[29] The T_C and coercive field (H_C) of Cr-doped $(\text{Bi,Sb})_2\text{Te}_3$


were significantly enhanced when it was coupled with CrSb antiferromagnet (AFM).^[30] The H_C of an Fe_3GeTe_2 (FGT) thin film was dramatically enhanced when it was coupled with MnTe .^[4] In addition, the recent works about proximity effects in graphene/2D and $\text{CrI}_3/\text{TaSe}_2$ FM heterostructures also provide us a direction to modulate and control the magnetic properties in magnetic heterostructures.^[31–33]

Among the various types of 2D vdW FMs discovered, FGT is a promising material that possesses several distinct advantages: 1) its T_C is much higher than those of most other FMs, 2) it has been successfully grown to wafer size,^[4,16] and 3) the itinerant character of its electrons gives it the ability to be modulated sensitively through proximity coupling effects. Here, we fabricate FGT thin flakes and use vdW AFM FePS_3 (FPS) to enhance the magnetic performances of FGT through constructing FPS/FGT and FPS/FGT/FPS heterostructures. The magneto-optical Kerr effect (MOKE) results demonstrate that exchange bias effects together with the significantly enhancements of T_C and H_C of FGT have been observed in both FPS/FGT and FPS/FGT/FPS heterostructures, which could be attributed to the proximity coupling of FGT with FPS due to the modulation of the domains in FGT by FPS at the interfaces. This work makes 2D

L. M. Zhang, H. Dai, M. Wang, H. Cheng, Prof. X. Han, Prof. J. Han
Wuhan National High Magnetic Field Center and Department of Physics
Huazhong University of Science and Technology (HUST)
Wuhan 430074, P. R. China
E-mail: junbo.han@mail.hust.edu.cn

X. Y. Huang, L. Tong, Z. Li, Prof. L. Ye
School of Optical and Electronic Information and Wuhan National
Laboratory for Optoelectronics
Huazhong University of Science and Technology
Wuhan 430074, P. R. China
E-mail: leiye@hust.edu.cn

Prof. X. Wang
School of Mathematics and Physics
Wenhua College
Wuhan 430074, P. R. China

 The ORCID identification number(s) for the author(s) of this article can be found under <https://doi.org/10.1002/adma.202002032>.

DOI: 10.1002/adma.202002032

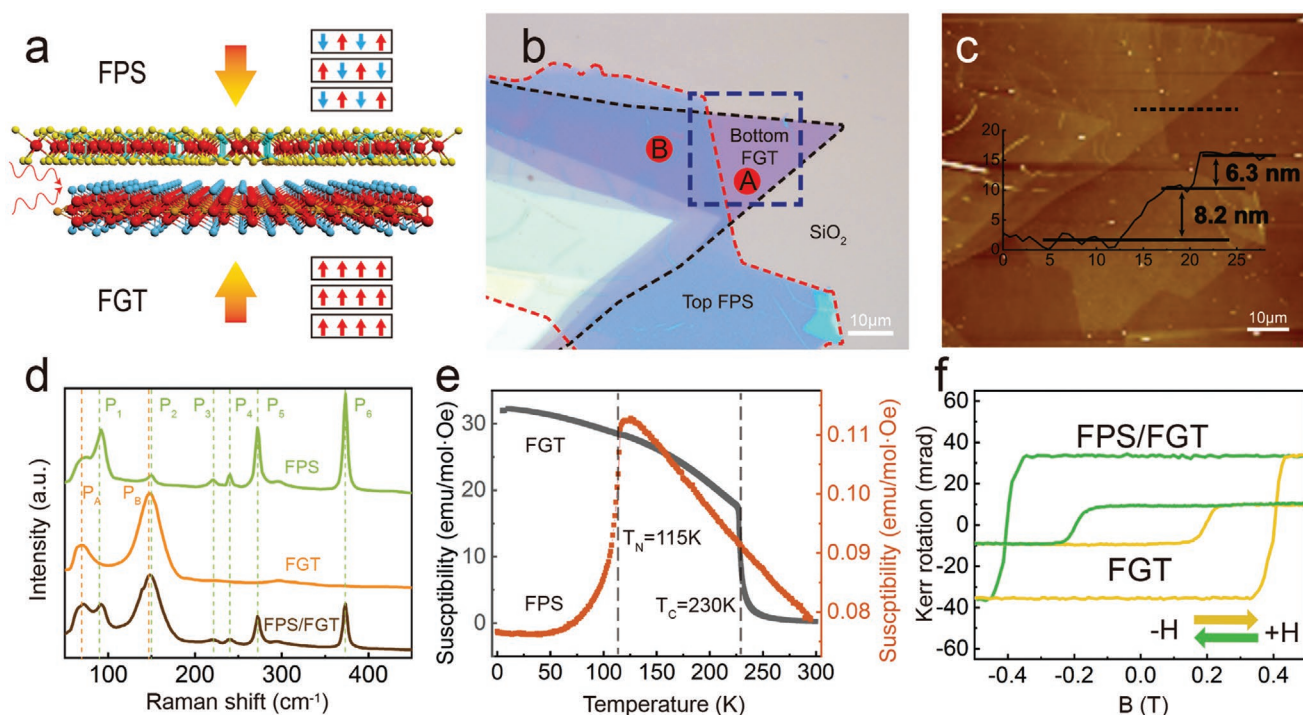


Figure 1. a) Magnetic ordering in vdW FGT and FPS thin flakes. b) Optical image of the FPS/FGT heterostructure formed by stacking FPS (top) on FGT (bottom). c) Atomic force microscopy image of the FPS/FGT heterostructure shown in (b), with the inset showing the thicknesses of the FGT (8.2 nm) and FPS (6.3 nm) layers along the dashed line. d) Raman spectra of FPS, FGT, and the FPS/FGT heterostructure (stacked area). Six peaks from FPS and two peaks from FGT were observed, while no obvious additional peak was observed from the stacked area. e) Magnetic susceptibility as a function of temperature for FGT (gray curve) and FPS (orange curve) single crystals along the *c*-axis. The *T_C* of FGT and the Neel temperature (*T_N*) of FPS were extracted as 230 and 115 K, respectively. f) Typical MOKE signal for an FGT flake and an FPS/FGT heterostructure measured at 80 K.

ultrathin FPS/FGT and FPS/FGT/FPS heterostructures promising candidates for applications in magnetic sensors, magnetic switching, and storage devices.^[9,34,35]

FGT and FPS single crystals were grown using the chemical vapor transport method and confirmed by the X-ray diffraction (XRD) technique and scanning electron microscope (SEM, see Section S1, Supporting Information). The basic magnetic properties of FGT and its coupling with substrates have been investigated in our previous work^[36] and no magnetic enhancement has been observed in FGT on any of the three substrates utilized. To enhance the magnetic properties (including the *T_C* and *H_C*) of FGT, vdW AFM FPS flakes were used to construct FPS/FGT bilayer heterostructures (BHS) and three samples, named BHS-1, BHS-2, and BHS-3, were prepared and characterized to confirm the universality of the enhancement effects (see Section S2, Supporting Information). **Figure 1** demonstrates the magnetic and optical properties of the FPS/FGT heterostructure and its components. Figure 1a shows the schematic of the FPS/FGT heterostructure composed of FGT and FPS. FGT has a ferromagnetic order, while FPS is an Ising-type AFM with both intra- and interlayer antiferromagnetic orders. Figure 1b presents a typical optical image of the FPS/FGT heterostructure (BHS-1), wherein a large piece of thin FPS is stacked onto the surface of an FGT flake. As shown in the atomic force microscopy image given in Figure 1c, the thicknesses of FGT and FPS were 8.2 and 6.3 nm, respectively. To ensure the quality of BHS-1, both energy-dispersive spectroscopy (EDS) and Raman scattering

techniques were used to characterize BHS-1 in different locations (see Section S2, Supporting Information). All the elements, including Fe, Ge, Te, P, and S, could be observed in the stacked area of the device, and the Raman signatures at room temperature show that both FGT and FPS layers in the stacked area are identical to the individual layers, and no additional new peaks were observed for the stacked areas (see Figure 1d).

Figure 1e shows the temperature-dependent magnetic susceptibility curves of FGT and FPS single crystals measured with the magnetic field along the *c* axes of the crystals under the cooling field of 100 Oe. The intrinsic ferromagnetism of bulk FGT persists at temperatures lower than 230 K and the antiferromagnetic-to-paramagnetic phase transition of FPS bulk crystals occurs at ≈115 K. For the thin FGT and FPS flakes used in this heterostructure, the critical temperatures were characterized by MOKE and Raman techniques, respectively. Figure 1f gives the typical MOKE curves of the FPS/FGT heterostructure (BHS-3) and the FGT flakes taken from the unstacked part of the heterostructure at 80 K, in which rectangular magnetic loops could be observed for both parts. By varying the measurement temperature, the *T_C* value could be extracted. For FPS, the Neel temperature (*T_N*) could be extracted from the Raman shift data (see Figure S4, Supporting Information). For comparison, the MOKE curve of the stacked part taken under the same experimental conditions was also combined with that of FGT. Both the residual Kerr rotation (*θ_K*) and the *H_C* values of FPS/FGT were much larger than those of the individual FGT, which

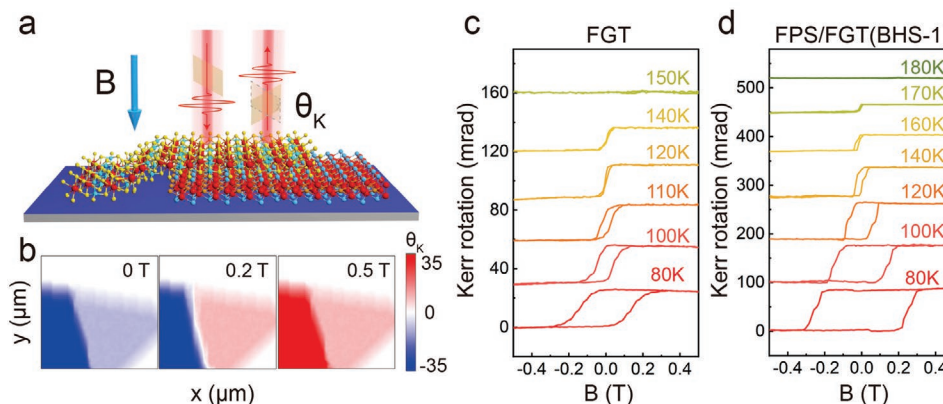


Figure 2. a) Schematic of the MOKE measurement of FPS/FGT heterostructure. b) MOKE map of a partial area in BHS-1 (framed area in Figure 1b). c,d) Comparison of the temperature-dependent Kerr rotation versus the magnetic field for pure FGT and the FPS/FGT in BHS-1.

means that FPS has great effect on the magnetic properties of FGT.

To evaluate the modulation effects of FPS on FGT, MOKE techniques were used to comparatively investigate the magnetic properties of FGT and FPS/FGT. **Figure 2a** shows the schematic of the MOKE system and the cartoon picture of FPS/FGT heterostructure. To obtain the out-of-plane ferromagnetism, a normal-irradiated 633 nm laser was used to detect the MOKE signals of the samples. During our experiments, two different measurement modes were utilized. For θ_K and H_C measurements at a given point (see point A for FGT and point B for FPS/FGT in Figure 1b), the Kerr loop was recorded with the magnetic field sweeping from -0.5 to 0.5 T. For the Kerr mapping measurement, the Kerr values of a given area were recorded point-by-point, with sample moved by a two-axis translation stage. Figure 2b shows the spatial maps of the Kerr rotation taken at 80 K with the magnetic fields fixed at 0, 0.2, and 0.5 T, respectively. (The mapping area is framed in Figure 1b.) It is clear that the FPS flake shows no MOKE signal, the Kerr intensity of the stacked part is much stronger than that of the pure-FGT part, and the θ_K value does not vary much inside the FPS/FGT or FGT regions.

To compare the magnetic properties of FGT and FPS/FGT and get more detailed information about the sample, temperature-dependent Kerr loops of FGT and FPS/FGT were measured and are given in Figure 2c,d, respectively. Several significant differences could be observed. First, the θ_K of the FPS/FGT structure was about three times larger than that of the pure FGT, while the corresponding H_C of FPS/FGT was almost double that of the pure FGT in the data taken at 80 K. Then, with the increase of the temperature, the hysteresis loop of the pure FGT shrank and then disappeared at ≈ 120 K, while it still existed for FPS/FGT until 160 K. Finally, the θ_K decreased to zero at 150 K for pure FGT and at 180 K for FPS/FGT. As a result, remarkable enhancements of θ_K , H_C , and T_C were observed in FPS/FGT.

To determine the coupling mechanism between FPS and FGT, the domain characters of FGT and FPS/FGT (BHS-1) were investigated, as shown in **Figure 3**. Figure 3a shows the MOKE signals of FGT and FPS/FGT taken at 80 K. Interestingly, the hysteresis loop of FPS/FGT demonstrates more

complicated structures than does that of pure FGT. Multiple magnetic states and exchange bias occur when FPS and FGT were coupled together, the spin textures in FGT endure significant influence by FPS through proximity coupling. To explain this phenomenon, both the domain orientations of FGT and FPS at the interface and the exchange bias caused by the proximity coupling effects were illustrated in Figure 3b. Different from the pure FGT that has only two stable magnetic states in the hysteresis loop, FPS/FGT heterostructure demonstrates four typical magnetic states (marked as 1–4 in Figure 3b). It is suitable to assume that for all of the four states, the orientations of the domains in FPS are hard to flip at the magnetic field variation range of ± 0.5 T, since it takes tens of tesla to flip the spin (or domain) inside AFM crystal (see Figure S5, Supporting Information).^[37] For states 1 and 3, the domain walls in FGT vanishes under saturated magnetic field. While for states 2 and 4, the orientation of some of the domains in FGT are parallel to the external magnetic field, while others are fixed to the domains in FPS due to the pinning effects caused by the proximity coupling, resulting in an inflexion in MOKE signal. Different from the single-shifted hysteresis loop observed in FGT/FPS and FGT/CrPS₃ systems,^[38] the curve here shows double-shifted hysteresis loops, which is a clear evidence of exchange bias effects. This phenomenon is common and usually observed in the zero-field cooled curves taken from AFM/FM systems where the T_C of FM is higher than T_N of AFM.^[39] The double-shifted loops could be divided into two single ones once the sample is demagnetized and then cooled under magnetic field.^[40] It should also be noticed that the exchange bias (H_{EX} and H_{EX}^-) shown in Figure 3b is small, but it could be enhanced when the measurement temperature was lowered down (see Figure S6, Supporting Information)^[39] or the AFM thickness was increased.^[40]

Figure 3c displays the extracted θ_K as a function of temperature for FGT and FPS/FGT, for which the data were fitted by the function $\alpha(1 - T/T_C)^\beta$. The fitted T_C is ≈ 150 K for FGT, while it is ≈ 180 K for FPS/FGT. Figure 3d displays the extracted H_C as a function of temperature for the two parts of this sample. θ_K and H_C showed remarkable enhancements when the FPS layer was stacked onto the FGT flake. Additionally, obvious enhancements of T_C and H_C as well as multiple magnetic states

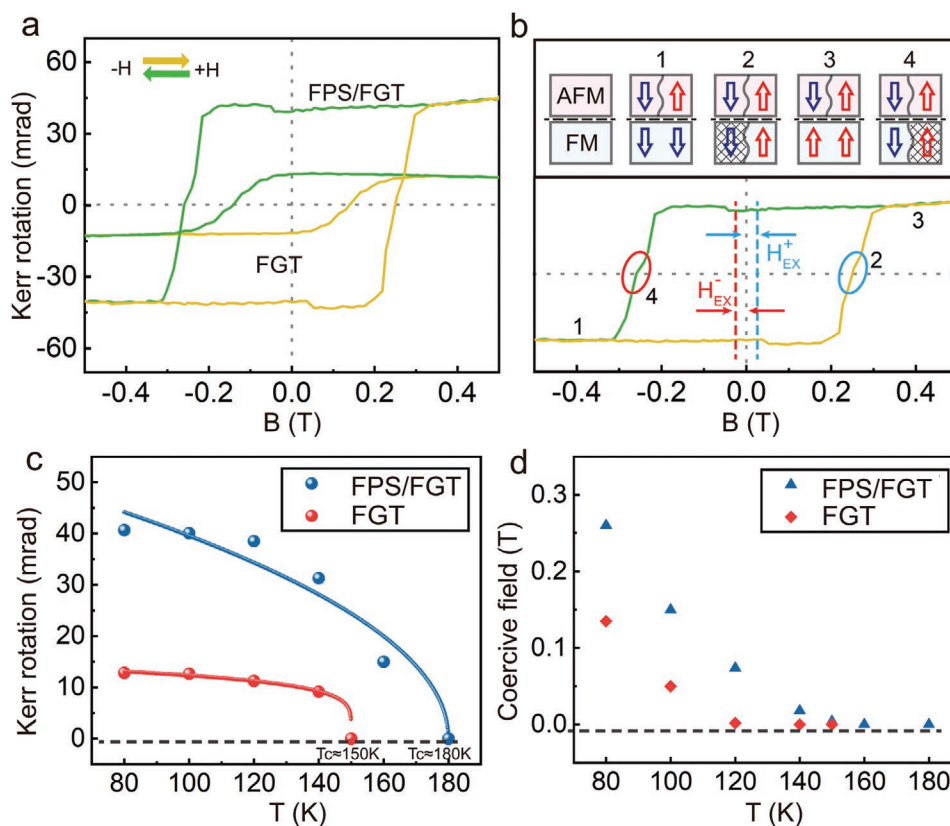


Figure 3. a) Comparison of the MOKE signals versus the magnetic field at 80 K for FGT and FPS/FGT. b) The domain of the FGT and FPS layers around the interface of FPS/FGT under the different external magnetic fields. The dashed line indicates the interface between FPS and FGT. The exchange bias fields were marked by H_{EX}^+ and H_{EX}^- . c) Extracted Kerr rotations as functions of the temperature for FGT (red curve) and FPS/FGT (blue curve), respectively. The dots are experimental data, while the solid lines are the fitting curves obtained using the function $\alpha(1 - T/T_C)^\beta$. d) Extracted H_C as a function of temperature for FGT (red dots) and FPS/FGT (blue dots).

were observed in BHS-2 (see Figure S7, Supporting Information). So far, we considered that the enhancements of T_C and H_C were from the proximity effect at the interface between FPS and FGT, which modifies the domain characters of FGT by FPS through pinning effect. Moreover, it is also worth noticing that the magnetic ordering characters of FPS was also modified by FGT during the cooling process, which resulted in a completely different temperature-dependent Raman shifting behaviors of P1 and P2 between pure FPS and FPS/FGT (see Figure S4, Supporting Information). The above results provide an effective method by which to obtain 2D materials with higher T_C values for magnetic spintronic devices and help in understanding the physics of proximity coupling between 2D FM and AFM.

To further explore the proximity effect in a double-interfacial system, two sandwiched structures (three-layer heterostructure (THS)) composed of FPS/FGT/FPS (THS-1 and THS-2) were fabricated and their magnetic properties were studied by MOKE measurements. The optical images and the corresponding temperature-dependent Kerr loops of THS-1 and THS-2 are shown in Figures S10–S12 in the Supporting Information. Obviously, the T_C of FPS/FGT/FPS was promoted by ≈ 35 K compared to that of pure FGT and H_C was also enhanced significantly. Figure 4a shows the comparison of the MOKE signals of pure FGT and FPS/FGT/FPS (THS-1) versus the magnetic field at 80 K. It is notable that the hysteresis loop also exhibited a two-step

process. Similar to the results shown in Figure 3, the hysteresis loop also showed a double-shift profile due to the exchange bias effects. Benefit from the double interfaces and thicker FPS layer in FPS/FGT/FPS, the exchange bias and the magnetic states (see Figure 4b) are much obvious than those of FPS/FGT.

The tendency of the Kerr rotation of FPS/FGT/FPS was quite different from that of the pure FGT. Figure 4c exhibits the extracted Kerr rotations of FGT and FPS/FGT/FPS versus temperature. Different from the curve of FGT, which could be fitted by a single function, $\alpha(1 - T/T_C)^\beta$, the curve of FPS/FGT/FPS was composed of two different components and needed to be fitted by the superposition of two $\alpha(1 - T/T_C)^\beta$ functions. Coincidentally, the extra extension (dashed line) of the lower-temperature part of the curve intersects with the x -axis right at the T_C point of the pure FGT. Figure 4d displays the extracted H_C as a function of temperature for FGT and FPS/FGT/FPS. The H_C of FPS/FGT/FPS was also twice higher than that of FGT at most of the temperatures. Additionally, THS-2 demonstrated the same feature as did THS-1 (shown in Figure S10, Supporting Information), which confirms the universality of the enhancement of T_C and H_C as well as the multiple magnetic states in FPS/FGT/FPS triply stacked structures.

So far, we have demonstrated that when FPS and FGT were stacked together, an exchange interaction occurred at the interfaces between AFM/FM and FM/AFM. The strong

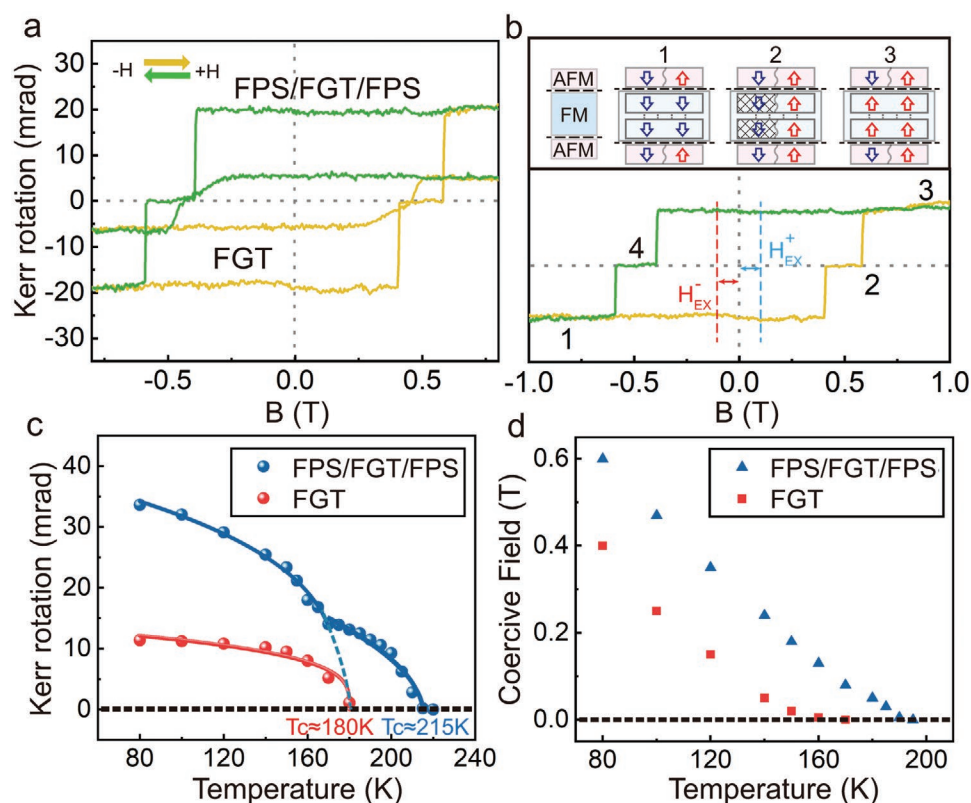


Figure 4. a) Comparison of the MOKE signals versus the magnetic field at 80 K for pure FGT and the FPS (top)/FGT (middle)/FPS (bottom) heterostructure. b) The domain of FPS (top)/FGT (middle)/FPS (bottom) at three typical magnetic states. The dashed line indicates the interface between FPS and FGT. The exchange bias fields were marked by H_{EX}^+ and H_{EX}^- . c) Extracted Kerr rotation as a function of temperature for FGT (red curve) and FPS/FGT/FPS (blue curve), with the solid lines showing fittings obtained using the function $\alpha(1 - T/T_C)^\beta$. d) Extracted H_C as a function of temperature for FGT (red dots) and FPS/FGT/FPS (blue dots).

exchange effects modified the domain of FGT at the interface and lead to an exhibition of exchange bias and multiple magnetic states in hysteresis loops, and the substantive enhancement of H_C and T_C for the FPS/FGT and FPS/FGT/FPS heterostructures. The origin of such exchange coupling is traditionally studied by neutron diffraction, but this method is hard to apply here due to the limitation of the short diffraction length. In addition, electrons transferring between FGT and FPS may also play important roles in enhancing the magnetic properties of FGT, which should be investigated in detail in the future.

In summary, we have demonstrated an effective way to enhance the ferromagnetism of 2D FGT through the proximity coupling of FPS with FGT. By constructing FPS/FGT and FPS/FGT/FPS heterostructures, the T_C of FGT was improved by 30 K in FPS/FGT and 35 K in FPS/FGT/FPS, while the H_C values were almost doubled. In addition, exchange bias and multiple magnetic states have been observed in FPS/FGT and FPS/FGT/FPS, which provides a way to understand the modulation of domains in FGT by FPS at the interfaces. Our works show that AFM–FM coupling is an effective way to strengthen itinerant ferromagnetism without consuming any external energy. It also provides a way to explore the domain dynamics of magnets through proximity coupling effects.

Experimental Section

Growth of Single Crystals: Both the FGT and FPS single crystals were grown by chemical vapor transport method. For FGT, the powers of Fe (99.999%), Ge (99.999%), and Te (99.999%) were mixed in a 3:1:2 ratio with appropriate iodine in N_2 -protection glove box, which were then immediately sealed into a quartz ampule at a pressure of ≈ 1 Pa. The quartz ampule was finally placed into a horizontal two-zone furnace with hot zone at 1023 K and cold zone at 923 K for one week and then cooled naturally. For FPS, powers of Fe (99.999%), P (99.999%), and S (99.999%) in a 1:1:3 ratio were used and grinded uniformly in N_2 -protection glove box. The mixture was then sealed into a quartz ampule with appropriate iodine. Finally, the ampule was placed into a horizontal two-zone furnace with hot zone at 953 K and cold zone at 873 K for eight days and cooled with 3 K min^{-1} to room temperature.

Fabrication of the FPS/FGT and FPS/FGT/FPS Heterostructures: The FPS/FGT and FPS/FGT/FPS van der Waals (vdW) heterostructures presented in this work were fabricated by a common dry transfer method utilizing a poly(dimethylsiloxane) (PDMS) carrier. For FPS/FGT, thin FGT flakes were exfoliated from the bulk counterparts using Scotch tape and then transferred onto a silicon substrate (with 300 nm SiO_2). Then, thin FPS flakes were exfoliated onto the PDMS film from an as-grown FPS crystal and transferred onto the FGT flake under the optical microscope assisted by an aligned transfer system. For FPS/FGT/FPS, an FPS flake with proper thickness was exfoliated from the bulk counterparts first and transferred onto SiO_2 substrate, then FGT flake were exfoliated and stacked onto the FPS flake by dry transfer method, finally another FPS flake was exfoliated from the bulk and stacked onto the top of FPS/FGT again.

Characterizations of the Single Crystals and the Heterostructures: The XRD and SEM equipped with an EDS were performed to check the quality, orientation, topography, and composition of the FGT and FPS single crystals respectively. The magnetization M of the ferromagnetic single crystal FGT and antiferromagnetic single crystal FPS were measured by a superconducting quantum interference device (SQUID) from 4.2 to 300 K with the magnetic field sweeping up to 9 T. The FPS/FGT vdW heterostructures were characterized by atomic force microscope, SEM, and EDS. Also, the temperature-dependent Raman measurements were performed in vacuum from liquid nitrogen temperature to room temperature using an optical cryostat in consideration of the degradation of samples. The 532 nm laser was focused onto samples by 50 \times microscope objective lens. The light spot was about 3 μ m. The laser power was kept below 100 μ W to avoid sample heating and the scattered signal was detected by a charge-coupled-device detector.

Magneto-Optic Kerr Effect (MOKE) Spectroscopy: The polar MOKE measurements were performed using a standard lab-made MOKE setup. A 633 nm polarized laser with the intensity of 3 μ W was used as a light source. The temperature range of the setup is 4.2–300 K, and the magnetic field range is 0–5 T. During the measurement, a chopper and a photoelastic modulator were used to improve the signal-to-noise ratio of the Kerr signal and the laser was irradiated normally on to the ab surface of the sample to detect the out-of-plane magnetism. Details of the optical setup are shown in Figure S8 in the Supporting Information.

Supporting Information

Supporting Information is available from the Wiley Online Library or from the author.

Acknowledgements

L.M.Z. and X.Y.H. contributed equally to this work. This project was supported by the National Scientific Foundation of China (Nos. 11704138, 61704061, and 11404124) and the Innovation team of Wenhua University (No. 2019T02). The authors thank the technical support from Analytical and Testing Center at Huazhong University of Science and Technology and the in-depth discussion of domain characters at the interface of FPS and FGT from Prof. Zhengcai Xia and Huahua Fu.

Conflict of Interest

The authors declare no conflict of interest.

Keywords

2D magnetic materials, enhanced coercive field, improved Curie temperature, proximity coupling, van der Waals heterostructures

Received: March 24, 2020

Revised: June 20, 2020

Published online:

- [1] B. Huang, G. Clark, E. Navarro-Moratalla, D. R. Klein, R. Cheng, K. L. Seyler, D. Zhong, E. Schmidgall, M. A. McGuire, D. H. Cobden, W. Yao, D. Xiao, P. Jarillo-Herrero, X. Xu, *Nature* **2017**, *546*, 270.
- [2] C. Gong, L. Li, Z. Li, H. Ji, A. Stern, Y. Xia, T. Cao, W. Bao, C. Wang, Y. Wang, Z. Q. Qiu, R. J. Cava, S. G. Louie, J. Xia, X. Zhang, *Nature* **2017**, *546*, 265.

- [3] D. J. O'Hara, T. Zhu, A. H. Trout, A. S. Ahmed, Y. K. Luo, C. H. Lee, M. R. Brenner, S. Rajan, J. A. Gupta, D. W. McComb, R. K. Kawakami, *Nano Lett.* **2018**, *18*, 3125.
- [4] S. Liu, X. Yuan, Y. Zou, Y. Sheng, C. Huang, E. Zhang, J. Ling, Y. Liu, W. Wang, C. Zhang, J. Zou, K. Wang, F. Xiu, *npj 2D Mater. Appl.* **2017**, *1*, 30.
- [5] M. Bonilla, S. Kolekar, Y. Ma, H. C. Diaz, V. Kalappattil, R. Das, T. Eggers, H. R. Gutierrez, M. H. Phan, M. Batzill, *Nat. Nanotechnol.* **2018**, *13*, 289.
- [6] Z. Fei, B. Huang, P. Malinowski, W. Wang, T. Song, J. Sanchez, W. Yao, D. Xiao, X. Zhu, A. F. May, W. Wu, D. H. Cobden, J. H. Chu, X. Xu, *Nat. Mater.* **2018**, *17*, 778.
- [7] H. Haugen, D. Huertas-Hernando, A. Brataas, *Phys. Rev. B* **2008**, *77*, 115406.
- [8] Z. Wang, D. Sapkota, T. Taniguchi, K. Watanabe, D. Mandrus, A. F. Morpurgo, *Nano Lett.* **2018**, *18*, 4303.
- [9] M. Alghamdi, M. Lohmann, J. Li, P. R. Jothi, Q. Shao, M. Aldosary, T. Su, B. P. T. Fokwa, J. Shi, *Nano Lett.* **2019**, *19*, 4400.
- [10] D. Zhong, K. L. Seyler, X. Linpeng, R. Cheng, N. Sivadas, B. Huang, E. Schmidgall, T. Taniguchi, K. Watanabe, M. A. McGuire, W. Yao, D. Xiao, K. C. Fu, X. Xu, *Sci. Adv.* **2017**, *3*, e1603113.
- [11] T. Song, X. Cai, M. W. Tu, X. Zhang, B. Huang, N. P. Wilson, K. L. Seyler, L. Zhu, T. Taniguchi, K. Watanabe, M. A. McGuire, D. H. Cobden, D. Xiao, W. Yao, X. Xu, *Science* **2018**, *360*, 1214.
- [12] B. Huang, G. Clark, D. R. Klein, D. MacNeill, E. Navarro-Moratalla, K. L. Seyler, N. Wilson, M. A. McGuire, D. H. Cobden, D. Xiao, W. Yao, P. Jarillo-Herrero, X. Xu, *Nat. Nanotechnol.* **2018**, *13*, 544.
- [13] Z. Wang, I. Gutierrez-Lezama, N. Ubrig, M. Kroner, M. Gibertini, T. Taniguchi, K. Watanabe, A. Imamoglu, E. Giannini, A. F. Morpurgo, *Nat. Commun.* **2018**, *9*, 2516.
- [14] W. Y. Xing, Y. Y. Chen, P. M. Odenthal, X. Zhang, W. Yuan, T. Su, Q. Song, T. Y. Wang, J. N. Zhong, S. Jia, X. C. Xie, Y. Li, W. Han, *2d Mater.* **2017**, *4*, 024009.
- [15] Z. Wang, T. Zhang, M. Ding, B. Dong, Y. Li, M. Chen, X. Li, J. Huang, H. Wang, X. Zhao, Y. Li, D. Li, C. Jia, L. Sun, H. Guo, Y. Ye, D. Sun, Y. Chen, T. Yang, J. Zhang, S. Ono, Z. Han, Z. Zhang, *Nat. Nanotechnol.* **2018**, *13*, 554.
- [16] Y. Deng, Y. Yu, Y. Song, J. Zhang, N. Z. Wang, Z. Sun, Y. Yi, Y. Z. Wu, S. Wu, J. Zhu, J. Wang, X. H. Chen, Y. Zhang, *Nature* **2018**, *563*, 94.
- [17] T. Song, Z. Fei, M. Yankowitz, Z. Lin, Q. Jiang, K. Hwangbo, Q. Zhang, B. Sun, T. Taniguchi, K. Watanabe, M. A. McGuire, D. Graf, T. Cao, J. H. Chu, D. H. Cobden, C. R. Dean, D. Xiao, X. Xu, *Nat. Mater.* **2019**, *18*, 1298.
- [18] T. Li, S. Jiang, N. Sivadas, Z. Wang, Y. Xu, D. Weber, J. E. Goldberger, K. Watanabe, T. Taniguchi, C. J. Fennie, K. Fai Mak, J. Shan, *Nat. Mater.* **2019**, *18*, 1303.
- [19] P. Lazic, K. D. Belashchenko, I. Zutic, *Phys. Rev. B* **2016**, *93*, 241401.
- [20] Y. G. Semenov, K. W. Kim, J. M. Zavada, *Appl. Phys. Lett.* **2007**, *91*, 153105.
- [21] B. Scharf, A. Matos-Abiad, J. E. Han, E. M. Hankiewicz, I. Zutic, *Phys. Rev. Lett.* **2016**, *117*, 166806.
- [22] P. Wei, S. Lee, F. Lemaitre, L. Pinel, D. Cutaia, W. Cha, F. Katmis, Y. Zhu, D. Heiman, J. Hone, J. S. Moodera, C.-T. Chen, *Nat. Mater.* **2016**, *15*, 711.
- [23] Z. Wang, C. Tang, R. Sachs, Y. Barlas, J. Shi, *Phys. Rev. Lett.* **2015**, *114*, 016603.
- [24] S. Singh, J. Katoch, T. Zhu, K. Y. Meng, T. Liu, J. T. Brangham, F. Yang, M. E. Flatte, R. K. Kawakami, *Phys. Rev. Lett.* **2017**, *118*, 187201.
- [25] S. Y. Huang, X. Fan, D. Qu, Y. P. Chen, W. G. Wang, J. Wu, T. Y. Chen, J. Q. Xiao, C. L. Chien, *Phys. Rev. Lett.* **2012**, *109*, 107204.
- [26] Y. C. Lau, D. Betto, K. Rode, J. M. Coey, P. Stamenov, *Nat. Nanotechnol.* **2016**, *11*, 758.

- [27] F. Maccherozzi, M. Sperl, G. Panaccione, J. Minar, S. Polesya, H. Ebert, U. Wurstbauer, M. Hochstrasser, G. Rossi, G. Woltersdorf, W. Wegscheider, C. H. Back, *Phys. Rev. Lett.* **2008**, *101*, 267201.
- [28] S. H. Nie, Y. Y. Chin, W. Q. Liu, J. C. Tung, J. Lu, H. J. Lin, G. Y. Guo, K. K. Meng, L. Chen, L. J. Zhu, D. Pan, C. T. Chen, Y. B. Xu, W. S. Yan, J. H. Zhao, *Phys. Rev. Lett.* **2013**, *111*, 027203.
- [29] F. Katmis, V. Lauter, F. S. Nogueira, B. A. Assaf, M. E. Jamer, P. Wei, B. Satpati, J. W. Freeland, I. Eremin, D. Heiman, P. Jarillo-Herrero, J. S. Moodera, *Nature* **2016**, *533*, 513.
- [30] Q. L. He, X. Kou, A. J. Grutter, G. Yin, L. Pan, X. Che, Y. Liu, T. Nie, B. Zhang, S. M. Disseler, B. J. Kirby, W. Ratcliff Ii, Q. Shao, K. Murata, X. Zhu, G. Yu, Y. Fan, M. Montazeri, X. Han, J. A. Borchers, K. L. Wang, *Nat. Mater.* **2017**, *16*, 94.
- [31] D. Ghazaryan, M. T. Greenaway, Z. Wang, V. H. Guarochico-Moreira, I. J. Vera-Marun, J. Yin, Y. Liao, S. V. Morozov, O. Kristanovski, A. I. Lichtenstein, M. I. Katsnelson, F. Withers, A. Mishchenko, L. Eaves, A. K. Geim, K. S. Novoselov, A. Misra, *Nat. Electron.* **2018**, *1*, 344.
- [32] B. Karpiak, A. W. Cummings, K. Zollner, M. Vila, D. Khokhriakov, A. M. Hoque, A. Dankert, P. Svedlindh, J. Fabian, S. Roche, S. P. Dash, *2D Mater.* **2019**, *7*, 015026.
- [33] M. Kim, P. Kumaravadivel, J. Birkbeck, W. Kuang, S. G. Xu, D. G. Hopkinson, J. Knolle, P. A. McClarty, A. I. Berdyugin, M. Ben Shalom, R. V. Gorbachev, S. J. Haigh, S. Liu, J. H. Edgar, K. S. Novoselov, I. V. Grigorieva, A. K. Geim, *Nat. Electron.* **2019**, *2*, 457.
- [34] J. M. Marmolejo-Tejada, K. Dolui, P. Lazic, P. H. Chang, S. Smidstrup, D. Stradi, K. Stokbro, B. K. Nikolic, *Nano Lett.* **2017**, *17*, 5626.
- [35] K. Dolui, M. D. Petrovic, K. Zollner, P. Plechac, J. Fabian, B. K. Nikolic, *Nano Lett.* **2020**, *20*, 2288.
- [36] L. Zhang, L. Song, H. Dai, J.-H. Yuan, M. Wang, X. Huang, L. Qiao, H. Cheng, X. Wang, W. Ren, X. Miao, L. Ye, K.-H. Xue, J.-B. Han, *Appl. Phys. Lett.* **2020**, *116*, 042402.
- [37] A. R. Wildes, D. Lançon, M. K. Chan, F. Weickert, N. Harrison, V. Simonet, M. E. Zhitomirsky, M. V. Gvozdkova, T. Ziman, H. M. Rønnow, *Phys. Rev. B* **2020**, *101*, 024415.
- [38] P. K. Srivastava, Y. Hassan, H. Ahn, B. Kang, S. G. Jung, Y. Gebredingle, M. Joe, M. S. Abbas, T. Park, J. G. Park, K. J. Lee, C. Lee, *Nano Lett.* **2020**, *20*, 3978.
- [39] S. Bruck, J. Sort, V. Baltz, S. Surinach, J. S. Munoz, B. Dieny, M. D. Baro, J. Nogues, *Adv. Mater.* **2005**, *17*, 2978.
- [40] X. H. Liu, K. W. Edmonds, Z. P. Zhou, K. Y. Wang, *Phys. Rev. Appl.* **2020**, *13*, 014059.